

A size-composition resolved aerosol model for simulating the dynamics of externally mixed particles: SCRAM (v 1.0)

Shupeng Zhu¹, Karine N. Sartelet¹, and Christian Seigneur¹

¹CEREA, joint laboratory Ecole des Ponts ParisTech - EDF R&D, Université Paris-Est, 77455 Champs-sur-Marne, France.

Correspondence to: S. Zhu
(zhus@cerea.enpc.fr)

Abstract. A Size-Composition Resolved Aerosol Model (SCRAM) for simulating the dynamics of externally-mixed atmospheric particles is presented. This new model classifies aerosols by both composition and size, based on a comprehensive combination of all chemical species and their mass-fraction sections. All three main processes involved in aerosol dynamics (coagulation, condensation/evaporation and nucleation) are included. The model is first validated by comparison with a reference solution and with results of simulations using internally-mixed particles. The degree of mixing of particles is investigated in a box model simulation using data representative of air pollution in Greater Paris. The relative influence on the mixing state of the different aerosol processes (condensation/evaporation, coagulation) and of the algorithm used to model condensation/evaporation (bulk equilibrium, dynamic) is studied.

1 Introduction

Increasing attention is being paid to atmospheric particulate matter (PM), which is a major contributor to air pollution issues ranging from adverse health effects to visibility impairment (EPA, 2009; Pascal et al., 2013). Concentrations of PM_{2.5} and PM₁₀ are regulated in many countries, especially in North America and Europe. For example, regulatory concentration thresholds of 12 and 20 $\mu\text{g m}^{-3}$ have been set for PM_{2.5} annual mass concentrations in the United States and Europe, respectively. Furthermore, particles influence the Earth's energy balance and global climate change (Myhre et al., 2013).

Three-dimensional chemical-transport models (CTM) are often used to study and forecast the formation and distribution of PM. The size distribution of particles is often discretised into sections

(e.g., Gelbard and Seinfeld, 1980; Zhang et al., 2004; Sartelet et al., 2007) or approximated by log-normal modes (e.g., Whitby and McMurry, 1997; Binkowski and Roselle, 2003). Moreover, CTM usually assume that particles are internally-mixed, i.e. each size section or log-normal mode has the same chemical composition, which may vary in space and time.

25 The internal-mixing assumption implies that particles of a same diameter (or in the same size section or log-normal mode) but originating from different sources have undergone sufficient mixing to achieve a common chemical composition for a given model grid cell and time. Although this assumption may be realistic far from emission sources, it may not be valid close to emission sources where the composition of new emitted particles can be very different from either background particles or
30 particles from other sources. Usually, internally- and externally-mixed particles are not differentiated in most measurements, which may be size-resolved (e.g., cascade impactors) but not particle specific (McMurry, 2000). The use of mass spectrometers for individual particle analysis has shed valuable information on the chemical composition of individual particles. Consequently, there is a growing body of observations indicating that particles are mostly externally mixed (e.g., Hughes et al., 2000;
35 Mallet et al., 2004; Healy et al., 2012; Deboudt et al., 2010).

The mixing state assumption may strongly influence aerosol chemistry and the hygroscopic characteristics of particles. Particles from different origins may not be well mixed, and their chemical composition may vary with their origins, leading to variations in their hygroscopic characteristics. This chemical identity of particles is gradually lost as the degree of mixing increases (or
40 completely lost under the internal mixing assumption). By influencing the hygroscopic characteristics of particles, the mixing state also influences the formation of secondary organic aerosols (SOA), because condensation/evaporation differs for species that are hydrophilic and/or hydrophobic (Couvidat et al., 2012). As the particle wet diameter is strongly related to the hygroscopic properties of particles, the mixing state also impacts particle wet diameters and the number of particles that
45 become cloud condensation nuclei (CCN), because the activation of particles into CCN is strongly related to the particle wet diameter (Leck and Svensson, 2014). By influencing CCN, the mixing state also affects aerosol wet removal and thus the aerosol spatial/temporal distribution. Besides, the mixing state influences the particle optical properties, which depend on both the particle size distribution (wet diameters) and composition (different chemical species possess different absorption/scattering properties). Lesins et al. (2002) found that the percentage difference in the optical properties between an internal mixture and external mixture of black carbon and ammonium sulphate can be over 50% for wet aerosols. The mixing state may also influence radiative forcing, as shown by Jacobson (2001) who obtained different direct forcing results between external and internal mixing simulations of black carbon.

55 Although CTM usually assume that particles are internally-mixed, several models have been developed during the last sesquidecade to represent the external mixture of particles. A source-oriented model was developed by Kleeman et al. (1997) and Kleeman and Cass (2001) for regional mod-

elling. In these models, each source is associated with a specific aerosol population, which may evolve in terms of size distribution and chemical composition, but does not mix with the other 60 sources (i.e., particle coagulation is neglected). Riemer et al. (2009) modelled externally-mixed particles using a stochastic approach. However, such an approach is computationally expensive when the number of particle species is high. On the other hand, Stier et al. (2005) and Bauer et al. (2008) simulate externally mixed particles using modal aerosol models, where aerosol populations with different mixing states are represented by modes of different compositions (soluble/mixed or insoluble/not mixed). Although these models may be computationally efficient, they may not model accurately 65 the dynamics of mixing. To represent externally-mixed particles independently of their sources and number concentrations, Jacobson et al. (1994) and Lu and Bowman (2010) considered particles that can be either internally- or externally-mixed (i.e., composed of a pure chemical species). Lu and Bowman (2010) used a threshold mass fraction to define whether the species is of significant 70 concentration. Jacobson (2002) expanded on Jacobson et al. (1994) by allowing particles to have different mass fractions. Similarly, Oshima et al. (2009) discretised the fraction of black carbon in the total particle mass into sections of different chemical compositions. Dergaoui et al. (2013) further expanded on these modelling approaches by discretising the mass fraction of any chemical species into sections, as well as the size distribution (see Section 2.1.3 for details). Based on this 75 discretisation, Dergaoui et al. (2013) derived the equation for coagulation and validated their model by comparing the results obtained for internal and external mixing, as well as by comparing both approaches against an exact solution. However, processes such as condensation/evaporation and nucleation were not modelled.

This work presents a new Size-composition Resolved Aerosol Model (SCRAM), which expands 80 on the model of Dergaoui et al. (2013) by including condensation/evaporation and nucleation processes. Section 2 describes the model. Equations for the dynamic evolution of particles by condensation/evaporation are derived. A thermodynamic equilibrium method may be used in SCRAM to compute the evolution of the particle chemical composition by condensation/evaporation. Redistribution algorithms, which allow section bounds not to vary, are also presented for future 3D 85 applications. Model validation is presented in Section 3 by comparing the changes in the particle size distribution due to condensational growth for both externally- and internally-mixed particles. Section 4 presents an application of the model with realistic concentrations over Greater Paris.

2 Model Description

This section presents the aerosol general dynamic equations and the structure of the model. First, 90 the formulation of the dynamic evolution of the aerosol size distribution and chemical composition by condensation-evaporation is introduced. Since it is necessary in 3D CTM to maintain fixed size and composition section bounds, we present algorithms to redistribute particle mass and number

according to fixed section bounds. For computational efficiency, a bulk equilibrium method, which assumes an instantaneous equilibrium between the gas and particle phases, is introduced. Finally, 95 the overall structure of the model is described. In particular, the treatment of the different mixing processes to ensure the numerical stability of the model is discussed.

Particle dynamics is mostly governed by three processes: coagulation, condensation/evaporation, and nucleation. Nucleation refers to the formation of ultra fine particles from gaseous molecules. SCRAM uses the parametrisation of Vehkamäki et al. (2002) for the homogeneous binary nucleation 100 of sulphate and water. It was adopted from the existing SIREAM code (Debry et al., 2007). It may be replaced by a better parametrisation in future versions, because it may lead to unrealistic results under some extreme conditions (Zhang et al., 2010). For coagulation, SCRAM uses the code of Dergaoui et al. (2013) to simulate the collisions of particles caused by Brownian motion. Condensation/evaporation describe the mass transfer process between the gas and the particle phases. It 105 is essential to include condensation/evaporation, because this process not only largely influences the size distribution of aerosols, but may also change the composition of particles significantly.

2.1 Condensation-Evaporation Algorithm

The focus of the following subsections is the formulation and implementation of the condensation/evaporation process. A lagrangian approach is used to solve the equations of change for the 110 mass and number concentrations, which are redistributed onto fixed sections through a redistribution algorithm (moving diameter, Jacobson (1997)). Equations are derived to describe the change with time of the mass concentrations of chemical species in terms of particle compositions.

2.1.1 Dynamic equation for condensation/evaporation

Let us denote m_i the mass concentration of species X_i ($1 \leq i \leq c$) in a particle and \mathbf{x} the vector 115 representing the mass composition of the particle $\mathbf{x} = (m_1, m_2, \dots, m_c)$. Following Riemer et al. (2009), the change with time of the number concentration $n(\mathbf{x}, t)$ ($\text{m}^{-3} \mu\text{g}^{-1}$) of multi-species particles by condensation/evaporation can be represented by the following equation:

$$\frac{\partial n}{\partial t} = - \sum_{i=1}^c \frac{\partial (I_i n)}{\partial m_i} \quad (1)$$

where I_i ($\mu\text{g s}^{-1}$) is the mass transfer rate between the gas and particle phases for species X_i . It may 120 be written as follows:

$$I_i = \frac{\partial m_i}{\partial t} = 2\pi D_i^g d_p f(K_n, \alpha_i) (c_i^g(t) - K_e(d_p) c_i^{eq}(\mathbf{x}, t)) \quad (2)$$

where D_i^g is the molecular diffusivity of condensing/evaporating species in the air, and d_p and c_i^g are the particle wet diameter and the gas phase concentration of species X_i , respectively. Non-continuous effects are described by $f(K_n, \alpha_i)$ (Dahneke, 1983) which depends on the Knudsen

125 number, $K_n = \frac{2\lambda}{d_p}$ (with λ the air mean free path), and on the accommodation coefficient $\alpha_i = 0.5$:

$$f(K_n, \alpha_i) = \frac{1 + K_n}{1 + 2K_n(1 + K_n)/\alpha_i} \quad (3)$$

$K_e(d_p)$ represents the Kelvin effect (for ultra fine particles, the curvature tends to inhibit condensation):

$$K_e(d_p) = \exp\left(\frac{4\sigma v_p}{R T d_p}\right) \quad (4)$$

130 with R the ideal gas constant, σ the particle surface tension and v_p the particle molar volume. The local equilibrium gas concentration c_i^{eq} is computed using the reverse mode of the thermodynamic model ISORROPIA V1.7 (Nenes et al., 1998) for inorganic compounds. In the current version of SCRAM, organic compounds are assumed to be at thermodynamic equilibrium with the gas phase and condensation/evaporation is computed as described in Section 2.2.

135 2.1.2 Dynamic equation as a function of mass fractions

Following the composition discretisation method of Dergaoui et al. (2013) (detailed in Section 2.1.3), each particle is represented by a vector $\mathbf{p} = (f, m)$, which contains the mass fraction vector $\mathbf{f} = (f_1, f_2, \dots, f_{(c-1)})$ of the first $(c-1)$ species and the total mass $m = \sum_{i=1}^c m_i$.

140 In Equation (1), the chemical composition of particles is described by the vector \mathbf{x} , which contains the mass concentration of each species. After the change of variable through a $[c \times c]$ Jacobian matrix from $n(\mathbf{x}, t)$ to $\bar{n}(\mathbf{p}, t)$ (see Appendix A for detail), Equation (1) becomes:

$$\frac{\partial \bar{n}}{\partial t} = - \sum_{i=1}^{(c-1)} \frac{\partial (H_i \bar{n})}{\partial f_i} - \frac{\partial (I_0 \bar{n})}{\partial m} \quad (5)$$

with $I_0 = \sum_{i=1}^c I_i$, $H_i = \frac{\partial f_i}{\partial t}$. As $f_i = \frac{m_i}{m}$ is the mass fraction of species (or group of species) X_i , we may write:

$$145 \quad H_i = \frac{1}{m} \frac{\partial m_i}{\partial t} - \frac{m_i}{m^2} \frac{\partial m}{\partial t} = \frac{I_i - f_i I_0}{m} \quad (6)$$

The change with time of $q_i = n m_i$, the mass concentration of species X_i , can be expressed as follows:

$$\frac{\partial q_i}{\partial t} = \frac{\partial n}{\partial t} m_i + \frac{\partial m_i}{\partial t} n \quad (7)$$

After the change of variables from $q_i(\mathbf{x}, t)$ to $\bar{q}_i(\mathbf{p}, t)$ (see Appendix A), Equation (7) becomes:

$$150 \quad \frac{\partial \bar{q}_i}{\partial t} = -m f_i \frac{\partial \bar{n}}{\partial t} + \bar{n} I_i \quad (8)$$

2.1.3 Discretisation

As SCRAM is a size-composition resolved model, both particle size and composition are discretised into sections, while the numbers and bounds of both size and composition sections can be customised by the user. The particle mass distribution $Q[m_{min}, m_{max}]$ is first divided into N_b size sections

155 $[m_k^-, m_k^+]$ ($k = 1, \dots, N_b$ and $m_{k-1}^+ = m_k^-$), defined by discretising particle diameters $[d_{min}, d_{max}]$ with d_{min} and d_{max} , the lower and upper particle diameters, respectively, and $m_k = \frac{\pi \rho d_k^3}{6}$. For each of the first $(c-1)$ species or species groups, the mass fraction is discretised into N_f fraction ranges. The h^{th} fraction range is represented by the range $F_h^- = [f_h^-, f_h^+]$ where $f_{h-1}^+ = f_h^-$, $f_{min} = 0$ and $f_{max} = 1$. Within each size section k , particles are categorised into N_p composition sections, which are defined by the valid combinations of the fraction ranges of the $(c-1)$ species. The g^{th} composition section can be represented by $\mathbf{P}_g = (F_{g1}^-, F_{g2}^-, \dots, F_{gc-1}^-)$. Given the mass fraction discretisation, those composition sections are automatically generated by an iteration on all possible combinations $(N_f)^{(c-1)}$ of the $(c-1)$ species and N_f fraction ranges. Only the composition sections that satisfy $\sum_{i=1}^{(c-1)} F_{gi}^- \leq 1$ are kept.

160 165 The particle mass distribution is discretised into $(N_b \times N_p)$ sections. Each section j ($j = 1, \dots, N_b \times N_c$) corresponds to a size section k ($k = 1, \dots, N_b$) and to a composition section $g = (g_1, \dots, g_{(c-1)})$ with $g = 1, \dots, N_p$, $g_h = 1, \dots, N_f$ with $h = 1, \dots, (c-1)$. The total concentration Q_i^j of species i in the j^{th} section can be calculated as follows:

$$Q_i^j = \int_{m_k^-}^{m_k^+} \int_{f_{g_1}^-}^{f_{g_1}^+} \dots \int_{f_{g_{(c-1)}}^-}^{f_{g_{(c-1)}}^+} \bar{q}_i(m, f_{g_1}, \dots, f_{g_{(c-1)}}) dm df_{g_1} \dots df_{g_{(c-1)}} \quad (9)$$

170 175 Similarly, the number concentration N^j of the j^{th} section may be written as follows:

$$N^j = \int_{m_k^-}^{m_k^+} \int_{f_{g_1}^-}^{f_{g_1}^+} \dots \int_{f_{g_{(c-1)}}^-}^{f_{g_{(c-1)}}^+} \bar{n}(m, f_{g_1}, \dots, f_{g_{(c-1)}}) dm df_{g_1} \dots df_{g_{(c-1)}} \quad (10)$$

After a series of derivations (see Appendix B for details), we obtain the time derivation of Equation (10):

$$\frac{\partial N^j}{\partial t} = 0 \quad (11)$$

175 as well as the time derivation of Equation (9):

$$\frac{\partial Q_i^j}{\partial t} = N^j I_{g_i} \quad (12)$$

Thus, in each section, the change with time of number and mass concentrations is given by Equations (11) and (12).

2.1.4 Numerical implementation

180 According to Debry and Sportisse (2006), the condensation/evaporation process may have characteristic time-scales of different magnitudes, because the range of particle diameters is large. Such feature induces strong stiffness of the numerical system. As suggested by Debry et al. (2007), the stiff condensation/evaporation equations are solved using the second-order Rosenbrock (ROS2) method (Verwer et al., 1999; Djouad et al., 2002).

185 In addition, potentially unstable oscillations may occur when a dramatic change of the particle pH occurs. To address this issue, a species flux electro-neutrality constraint (Pilinis et al., 2000; Debry et al., 2007) is applied in SCRAM to ensure the numerical stability of the system.

2.1.5 Size and composition redistribution

190 By condensation/evaporation, the particles in each size section may grow or shrink. Because the bounds of size sections should be fixed for 3D applications, it is necessary to redistribute number and mass among the fixed size sections during the simulation after condensation/evaporation. Similarly, the chemical composition also evolves by condensation/evaporation and an algorithm is needed to identify the particle composition and redistribute it into the correct composition sections.

195 Two redistribution methods for size sections may be used in SCRAM: the HEMEN (Hybrid of Euler-Mass and Euler-Number) scheme of Devilliers et al. (2013) and the moving diameter scheme of Jacobson (1997). According to Devilliers et al. (2013), both redistribution methods may accurately redistribute mass and number concentrations.

200 The HEMEN scheme divides particle size sections into two parts: the number is redistributed for sections of mean diameter lower than 100 nm and mass is redistributed for sections of mean diameter greater than 100 nm. The section mean diameters are kept constant and mass concentrations are diagnosed for sections where number is redistributed, while number concentrations are diagnosed for sections where mass is redistributed. The advantage of this scheme is that it is more accurate for number concentrations over the size range where number concentrations are the highest and more accurate for mass concentrations where mass concentrations are the highest. In SCRAM, the 205 algorithm of Devilliers et al. (2013) was modified to take into account the fact that after condensation/evaporation, the diameter of a section may become larger than the upper bound of the next section. In that case, the mean diameter of the section after condensation/evaporation is used to diagnose in which fixed-diameter sections the redistribution is performed. This feature allows us to use larger time steps for condensation/evaporation before redistribution.

210 In the moving diameter method, although size section bounds are kept fixed, the representative diameter of each size section is allowed to vary. If, after condensation/evaporation, the diameter grows or shrinks outside section bounds, both the mass and number concentrations of the section are redistributed entirely into the new size sections bounding that diameter.

For the composition redistribution, a scheme based on the moving diameter method is applied (i.e., moving mass fraction). First, after condensation/evaporation, the mass fraction of each species is re-evaluated within each section. For each section, if the new composition does not match the section composition (i.e., if the mass fraction of each species does not fit into the mass fraction bounds of the species for that section), the section that has a composition that matches the new composition is identified, and both number and mass concentrations of each species are transferred to that section.

The composition redistribution is applied first, followed by the size redistribution for each of the composition sections.

2.2 Bulk equilibrium and hybrid approaches

Bulk equilibrium methods assume an instantaneous thermodynamic equilibrium between the gas and bulk-aerosol phases. For semi-volatile species, the mass concentration of both gas and bulk-aerosol phases after condensation/evaporation are obtained using the forward mode of ISORROPIA for inorganics and the H₂O model (Couvidat et al., 2012) for organics. Because time integration is not necessary, the computational cost is significantly reduced compared to the dynamic method. Weighting factors W are designed to distribute the semi-volatile bulk-aerosol mass across the aerosol distribution (Pandis et al., 1993). In SCRAM, for each semi-volatile species i , we redistribute the bulk aerosol evaporating or condensing mass, $\delta Q_i = Q_i^{\text{after bulk eq.}} - Q_i^{\text{before bulk eq.}}$, between the sections j , using factors that depend on the ratio of the mass transfer rate in the aerosol distribution (Equation 2). Because of the bulk equilibrium assumption, the driving force of $(c_i^g - K_e c_i^{eq})$ is assumed to be the same for all size and composition sections, and the weighting factors are as follows.

$$W_i^j = \frac{N_j d_p^j f(K_n, \alpha_i)}{\sum_{k=1}^{N_s} N_k d_p^k f(K_n, \alpha_i)} \quad (13)$$

where N_j is the number concentration of section j and d_p^j is the particle wet diameter of section j . In case of evaporation, these weighting factors may not be appropriate, as they may lead to over-evaporation of some species in some sections, i.e. $Q_i^j \text{ after bulk eq.} = Q_i^{\text{before bulk eq.}} + \delta Q_i \times W_i^j < 0$. In the case of over-evaporation, we use a weighting scheme that redistributes the total bulk aerosol mass rather than the bulk aerosol evaporating or condensing mass

$$W_i^j = \frac{Q_i^j}{\sum_{k=1}^{N_s} Q_i^k} \quad (14)$$

and $Q_i^j \text{ after bulk eq.} = Q_i^{\text{after bulk eq.}} \times W_i^j$.

In fact, due to their larger ratios between surface area and particle mass, small particles may reach thermodynamic equilibrium much faster than large particles. Particles of diameters larger than 1 μm could require hours or even days to achieve equilibrium (Wexler and Seinfeld, 1990), which makes the bulk equilibrium assumption inappropriate for them. In order to maintain both the computational efficiency of the equilibrium method and the accuracy of the dynamic one, a hybrid method

is adopted in SCRAM based on the work of Capaldo et al. (2000) and Debry and Sportisse (2006). This method uses the equilibrium method for small particles ($d_p < 1 \mu\text{m}$) and uses the dynamic 250 method to calculate the mass transfer for larger particles.

2.3 Overall time integration and operator splitting in SCRAM

In order to develop a system that offers both computational efficiency and numerical stability, we perform operator splitting for changes in number and mass concentrations with time due to emission, coagulation, condensation/evaporation and nucleation, as explained below.

255 Emissions are first evaluated with an emission time step, which is determined by the characteristic time-scales of emissions obtained from the ratio of emission rates to aerosol concentrations. The emission time step evolves with time to prevent adding too much emitted mass into the system within one time step. Within each emission time step, coagulation and condensation/evaporation/nucleation are solved and the splitting time step between coagulation and condensation/evaporation/nucleation 260 is forced to be lower than the emission time step. Time steps are obtained from the characteristic time steps of coagulation (t_{coag}) and condensation/evaporation/nucleation (t_{cond}). The larger of the time steps t_{coag} and t_{cond} determines the time step of splitting between coagulation and condensation/evaporation/nucleation. As coagulation is usually the slower process, the change due to coagulation is first calculated over its time step. Then, condensation/evaporation/nucleation are 265 solved simultaneously. The change due to condensation/evaporation/nucleation is calculated, using time sub cycles, starting with the sub time step t_{cond} . The next sub time step for condensation/evaporation/nucleation is estimated based on the difference between the first and second order results provided by the ROS2 solver. Redistribution is computed after each time step of splitting of coagulation and condensation/evaporation/nucleation.

270 When the bulk thermodynamic equilibrium approach is used to solve condensation/evaporation, coagulation then nucleation are solved after each emission time step. The resolution is done as previously explained, except that the dynamic condensation/evaporation solver is disabled: sub time steps are used to solve coagulation and nucleation during one emission time step. Condensation/evaporation is then solved using the bulk equilibrium approach and the redistribution process is applied after the 275 bulk equilibrium algorithm.

When the hybrid approach is used to solve condensation/evaporation, a time loop is added with a fixed time step of 600 s outside the emission time loop to compute bulk equilibrium condensation/evaporation for equilibrium sections. This additional time loop is designed to ensure that bulk equilibrium condensation/evaporation of equilibrium sections is not applied too often, so that the 280 dynamic condensation/evaporation of dynamic sections has time to evolve. Redistribution is applied after the bulk equilibrium algorithm. Within this time loop, the aerosol dynamics is solved as previously explained using the dynamic condensation/evaporation algorithm for dynamic size sections:

emissions are solved followed by coagulation and condensation/evaporation/nucleation. As in the fully dynamic approach, redistribution is applied after dynamic condensation/evaporation.

285 **3 Model validation**

To validate the model, the change with time of internally- and externally-mixed aerosol models are compared. The simulations use initial conditions for number and mass concentrations that are typical of a regional haze scenario, with a sulphuric acid condensation rate of $5.5 \mu\text{m}^3\text{cm}^{-3}$ per 12 hours (Seigneur et al., 1986; Zhang et al., 1999) (sulphuric acid vapour source of $0.46 \mu\text{m}^3\text{cm}^{-3}$ per hour).

Simulations were conducted for 12 h at a temperature of 298 K and a pressure of 1 atm. The original reference simulation (Seigneur et al., 1986; Zhang et al., 1999) was first reproduced for internally-mixed sulphate particles (redistribution is not applied). For the sake of comparison between internally- and externally-mixed simulations, half of the particles were assumed to consist of sulphate (species 1) and the other half of another species of similar physical properties as sulphate (species 2). For internal mixing, the initial particles are all 50% species 1 and 50% species 2; and for external mixing, half of the initial particles are 100% species 1 and the other half are 100% species 2. As both species have the same physical properties, for any given size section, the sum over all composition sections of number and mass concentrations of externally-mixed particles should equal the number and mass concentrations of the internally-mixed particles. Particles were discretised into 100 size sections and 10 composition sections for the externally-mixed case. Figure 1 shows the initial and final distributions for the number and volume concentrations as a function of particle diameters. Both the internally-mixed and externally-mixed results are presented in Figure 1, along with the reference results of Zhang et al. (1999) (500 size sections were used in the original reference simulation). For the externally-mixed simulation, the results were summed up over composition sections to obtain the distributions as a function of particle diameter. As expected, a good match is obtained between internal and external mixing distributions, with an almost 100% Pearson's correlation coefficient. Furthermore, the accuracy of the SCRAM algorithm is proved by the good match between the results of these simulations and the reference simulation of Zhang et al. (1999). In order to investigate the influence of the composition resolution on simulation results, two additional tests are conducted using 2 and 100 composition bins. The mean mass fraction of species 1 is computed for all particles within each size section, as well as their standard deviations. Figure 2 shows the size distribution of these statistics. The mean mass fraction is barely affected by the different composition resolutions as the condensation rate of sulphate is independent of the particle compositions. However, a different composition resolution does lead to different standard deviation distributions, as only particles with larger fraction difference ($d > 0.2\mu\text{m}$ for 2 compositions and $d > 0.09\mu\text{m}$ for 10 compositions) can be distinguished from each other under coarser composition resolutions.

Using the same initial conditions and sulphuric acid condensation rate, a second comparison test was performed, with both coagulation and condensation occurring for 12 hours. As the coagulation 320 algorithm requires size sections to have fixed bounds (Dergaoui et al., 2013), size redistribution was applied for both the internally- and externally-mixed cases using the HEMEN method. As in the first comparison test, Figure 3 shows that there is a good match between the internally- and externally- mixed distributions as a function of particle diameter (no reference simulation was available for these simulations). This test validates the algorithm of SCRAM to simulate jointly the coagulation 325 and condensation of externally-mixed particles.

The mixing states of both internally- and externally-mixed particles at the end of the simulations of the second test are shown in Figure 4. Sulphuric acid condenses to form particulate sulphate (species 1). During the simulation, pure species 2 particles mix with pure sulphate particles by coagulation and condensation of sulphuric acid. Figure 4 shows that, at the end of the simulation, the sulphate 330 mass fraction is greater for particles of lower diameters, because the condensation rate is greater for those particles. Particles with diameters greater than 10 μm remain unmixed. However, the external mixing state provides a more detailed mixing map, from which it is possible to distinguish mixed particles from unmixed ones and to trace the origin of each particle. In this test case where the effect of condensation dominates that of coagulation, most mixed particles are originally pure species 2 335 particles coated with newly condensed sulphuric acid (Figure 4).

4 Simulation with realistic concentrations

To test the impact of external mixing on aerosol concentrations, simulations of coagulation, condensation/evaporation and nucleation were performed with SCRAM using realistic ambient concentrations and emissions extracted from a simulation performed over Greater Paris for July 2009 340 during the MEGAPOLI (Megacities: Emissions, urban, regional and Global Atmospheric POLLution and climate effects, and Integrated tools for assessment and mitigation) campaign (Couvidat et al., 2013).

4.1 Simulation set-up

Data were extracted from one grid cell of the 3D simulation performed by Couvidat et al. (2013) over 345 Greater Paris. This surface grid cell was chosen because black carbon (BC) emissions are high in that location, due to high traffic emissions. Figure 5 shows the BC emission map at 2 UT, on 1 July 2009. The highest emission rate is located at the grid cell center of longitude and latitude (2.28° E, 48.88° N), which was selected here to extract the SCRAM simulation input data for emissions, background gas and aerosol concentrations, and initial meteorological conditions (temperature and 350 pressure). In the absence of specific information on individual particle composition, all initial aerosol

concentrations extracted from the database were assumed to be 100% mixed (i.e., aged background aerosols).

Simulations start at 2 UT (1 July 2009), i.e., just before the morning peak of traffic emissions, and last 12 hours. As our simulations are 0D, the transport of gases and particles and the deposition processes are not taken into account. Therefore, emissions accumulate, potentially leading to unrealistically high concentrations. To avoid this artifact, the duration of the emissions was limited to the first 40 min of simulation. This time duration is calculated using the average BC emission rate between 2 UT and 3 UT, so that BC emissions lead to an increase in BC concentrations equal to the difference between BC concentrations after and before the morning traffic peak, i.e., between 6 UT and 2 UT (Figure 6). Besides, gas-phase chemistry (such as SOA formation) is not included in SCRAM, and is expected to be solved separately using a gas-phase chemistry scheme. In the simulations of this work, organics originate either from initial conditions or they are emitted as semi-volatile organic compounds during the simulation. They partition between the gas and the aerosol phases by condensation/evaporation.

The size distribution ranging from 0.001 to 10 μm was discretised into 7 sections with bounds at 0.001, 0.005, 0.01, 0.0398, 0.1585, 0.6310, 2.5119, and 10 μm . As in Couvidat et al. (2013), 31 particulate species were included in our simulations. In order to reduce the computational cost of the externally-mixed simulations, these species were grouped into 5 groups based on their chemical nature, which influences the formation of particles and their optical properties. Black carbon, organic species, inorganic species and dust are separated. Although sulphate could be separated from nitrate and ammonium for optical properties or for comparisons to observations of mixing state (Healy et al., 2012), and although chloride and sodium could be grouped together in a marine environment, all inorganic species are grouped together here for the sake of simplicity. However, because the hydrophylic properties of the particles strongly influence their formation and cloud condensation nuclei, hydrophylic and hydrophobic organic species are separated. In summary, the hydrophilic inorganic group (HLI) contains five inorganic species (sodium, sulphate, nitrate, ammonium and chloride); the hydrophilic organic group (HLO) contains 9 hydrophilic surrogate organic species (BiA2D, BiA1D, BiA0D, GLYOXAL, MGLY, BiMT, BiPER, BiDER and BiMGA); the hydrophobic organic group (HBO) contains 14 hydrophobic surrogate organic species (AnBIP, AnBmP, BiBIP, BiBmP, BiNGA, NIT3, BiNIT, AnCLP, SOAIP, SOAmP, SOAhP, POAIP, POAmP and POAhP); the black carbon group (BC) contains only black carbon; and the dust group (DU) contains all the neutral particles made up of soil, dust and fine sand. Refer to Couvidat et al. (2012) for detailed nomenclature of the organic species. For each of the first four groups, the mass fraction of the group over the total mass is discretised into 3 mass fraction sections ([0.0, 0.2], [0.2, 0.8], [0.8, 1.0]), leading to 20 possible particle composition sections, as shown in Table 1. Among them, there are 5 unmixed particles and 15 mixed particles. Here unmixed is used in an approximate sense: it means that the mass fraction of one chemical component is high (between 0.8 and 1), while the mass fraction of the other

chemical components is low (between 0 and 0.2). The dust mass fraction is not discretised, as it is obtained by mass conservation. Note that although as an example we chose dust to be the group for 390 which mass fraction is not treated explicitly, another group could be chosen as the group for which mass fraction is not treated explicitly. If all groups need to have their mass fraction treated explicitly, additional composition sections for the last group should be added to the current composition list without any modification to the main structure of the program. The mass fraction of the last group would still be obtained by mass conservation, and the composition section of the particles would be 395 chosen depending on this mass fraction.

In each group, water may also be present, although it is not considered when computing the mass fractions (it is calculated separately with the thermodynamic equilibrium models).

The model memorizes the relationship between each species index and group index, and it stores the mass concentrations separately for each species within each size-composition sections. The total 400 mass concentration of each group is computed from the mass concentration of each species based on the species-group relations, allowing the computation of the mass fraction of each group.

4.2 Aerosol dynamics and mixing state

To understand how initial concentrations mix with emissions, four scenarios were simulated. In scenario (A), only emissions are taken into account in the simulation. Only coagulation is added to 405 emissions in scenario (B), while only condensation/evaporation(C/E) is added to emissions in scenario (C). In scenario (D), emissions and all the aerosol dynamic processes are taken into account including nucleation (however, nucleation was not activated during the simulation due to low sulphuric acid gas concentrations).

The mass and number distributions of each chemical composition after 12 hours of simulation are 410 shown in Figures 7 and 8 as a function of particle diameter, as well as their initial distributions in sub-figure (e). Bars with grayscale represent unmixed particles, while bars with colours are mixed particles. Each bar corresponds to a chemical composition index (CI). However, any CI with small number or mass concentrations are not really visible from the plot, so they are regrouped into mixed-other (for mixed CI) and unmixed-other (for unmixed CI) in the plot. The chemical compositions 415 and the CI value associated with colour bars are listed in Table 1. All emitted particles are unmixed: CI 1 (100% DU) into size section (4-6), CI 3 (100% BC) into size section (3-6). Emissions also involve POA and H_2SO_4 gas-phase emissions.

As shown by the simulation of scenario (A), emissions lead to high number concentrations of BC in the sections of low diameters (mostly below 0.631 μm) and to high mass concentrations of dust 420 and BC in the sections of high diameters (mostly above 0.631 μm).

The comparison of scenarios (A) and (B) shows that coagulation does not affect much mass concentrations, but significantly reduces the number concentrations of particles in the sections of diameters lower than 0.631 μm . Also, due to coagulation, small particles migrated to higher sections. For

example, Figure 8 shows the mixed particles CI 15 migrated from the third size section to the fourth size section, this might be a result of the coagulation between CI 3 particles in the third size section and the CI 14 in the fourth size section. Besides, coagulation between CI 5 particles in the third size section may also produce some part of CI 15 in the fourth size section.

As shown by the simulation of scenario (C), C/E leads to high mass and number concentrations of unmixed HBO (CI 6 – mass fraction of HBO (81.2%) above 80% (exact mass fraction of dominate group will be specific within the parentheses right after the group name here after)), increasing the amount of unmixed particles. Organic matter of low and medium volatilities is emitted in the gas phase following Couvidat et al. (2013). This organic matter condenses subsequently on well-mixed particles (CI 14 with mixed HLI (31%) and HBO (41%)), in sufficient amount to increase the mass fraction of HBO (81%) to over 80% and, therefore, transferring particles to the unmixed category CI 6 (these particles are not exactly unmixed since up to 20% may correspond to HLI (10%), but a finer composition resolution would be required to analyse their mixed characteristics). The condensation of organic matter on freshly emitted BC particles (CI 3) also occurs, as shown by the mixed BC (26%) and HBO (68%) particles (CI 5) which appear in the third and fourth size sections.

As shown by comparing scenarios (A) and (B) and scenarios (C) and (D), coagulation significantly reduces number concentrations. The mass concentrations of fine particles (diameters lower than 0.631 μm) are also reduced. Furthermore, the composition diversity increases. For example, as demonstrated by the difference between scenarios (C) and (D), newly mixed particles of CI 4 (between 20% and 80% of HBO (78% for size 4 and 73% for size 5)) are formed by the coagulation of unmixed particles from CI 6 with others within the fourth and fifth size sections.

Table 2 shows the percentage of mixed particles for each scenario based on both particle number and mass concentrations. It seems that large particles are better mixed than small particles as the mixing percentages of mass are always higher than those of number. However, this phenomenon is specific to this case study; it is caused by the assumption of all initial particles being internally mixed and the initial conditions dominating for large particles due to their low emissions and the short duration of the simulations.

The number/mass mixing percentages after emission only (scenario (A)) provide a baseline for the analysis of the three other scenarios. In scenario (A), 42% (resp. 83%) of the particle number (resp. mass) originates from initial conditions and is mixed, while the remaining particles are due to emissions and are unmixed. The comparison of scenarios (A) and (B) shows that coagulation increases the mixing percentages, especially for small particles of high number concentrations. The mass mixing percentages decrease in scenario (C) because the condensation of freshly emitted organic matter on large mixed particles leads to particles with a mass fraction of organic matter (HBO) higher than 80%, i.e. unmixed. When all aerosol dynamic processes are taken into account (scenario (D)), only 51% of particle number concentration and 76% of particle mass concentration are mixed. The mixing percentages are greater than those of scenario (C), as mixing increases by coagulation,

but the mass mixing percentage is lower than in scenario (A) (emissions only) because of the strong condensation of HBO emitted in the gas phase.

4.3 External versus internal mixing

To investigate the consequence of the internal mixing hypothesis, a simulation of scenario (D) (all aerosol dynamic processes are taken into account) is conducted by assuming all particles to be internally mixed. Externally- and internally-mixed 12-hour simulations lead to a similar total aerosol mass concentration after 12 h ($33.09 \mu\text{gm}^{-3}$ for internal mixing and $33.35 \mu\text{gm}^{-3}$ for external mixing) as well as to similar total number concentrations ($1.16 \times 10^{10} \text{ #m}^{-3}$ for internal mixing and $1.07 \times 10^{10} \text{ #m}^{-3}$ for external mixing). The number and the species mass distributions are also similar, although external mixing leads to slightly lower ammonium concentrations ($2.68 \mu\text{gm}^{-3}$ versus $2.70 \mu\text{gm}^{-3}$), slightly higher nitrate concentrations ($3.19 \mu\text{gm}^{-3}$ versus $3.03 \mu\text{gm}^{-3}$) and higher chloride concentrations ($0.36 \mu\text{gm}^{-3}$ versus $0.25 \mu\text{gm}^{-3}$).

Figure 7 (d) and (f) compares the mass distributions and compositions within each size section after 12 h of the internal and external mixing simulations. External mixing provides more detail about the particle mixing state, as within each size section particles have different compositions. For example, in the case of internal mixing, particles in size section 4 (diameter between $0.0398 \mu\text{m}$ and $0.1585 \mu\text{m}$) are all mostly hydrophobic organics (CI 4: HBO (76%) between 20% and 80%). The particle compositions are more detailed in the external mixing simulation: while less than half of the particles are mostly hydrophobic organics (HBO 78%) (CI 4) as in internal mixing, a large amount are unmixed particles (CI 6: HBO (82%) between 80% and 100%), and some are equally mixed with BC and hydrophobic organics (CI 5). In size section 5, as in the internal mixing simulation, mixed particles dominate (CI 14 - HLI 46%, HBO 36%), but many have a different composition (CI 4 and 5) and some are unmixed HBO 83% (CI 6), BC 91% (CI 3) and dust 90% (CI 1). For particles in size section 6, particles are mixed particles of CI 12 (HLI 54%, DU 29%), while external mixing also shows that some particles are unmixed (BC 99% (CI 3) and dust 98% (CI 1)) and there are CI 14 (HLI 46%, HBO 35%) particles that originated from size section 5 through coagulation.

4.4 Bulk equilibrium and hybrid approaches

Additional external mixing tests were conducted using the bulk equilibrium and hybrid approaches for C/E to evaluate both their accuracy and computational efficiency. In the hybrid approach, the lowest four sections are assumed to be at equilibrium (up to diameters of $0.1585 \mu\text{m}$), whereas the other sections undergo dynamic mass transfer between the gas and particle phases .

The accuracy of these approaches is evaluated by comparing the mass and number distributions after 12 hour simulations with the bulk equilibrium or the hybrid approaches to the mass and number distributions computed dynamically (see Figures 9 and 10).

495 For externally-mixed particles, the dynamic mass distribution is shown in Figure 7(c); the bulk equilibrium and hybrid mass distributions are shown in Figure 9(a) and Figure 9(c), respectively. The dynamic number distribution is shown in Figure 8(c); the bulk equilibrium and hybrid mass distributions are shown in Figure 10(a) and Figure 10(c), respectively. For internally mixed particles, the dynamic mass/number distributions are shown in Figures 9(d) / 10(d) and the bulk equilibrium mass/number distributions in Figures 9(b) / 10(b), respectively.

500 For internally-mixed particles, the comparisons between Figures 9(b) and 9(d) and between Figures 10(b) and 10(d) indicate that the bulk equilibrium approach leads to significantly different distributions and compositions than the dynamic approach. This result also holds for externally-mixed particles, as shown by the comparisons between Figures 7(c) and 9(a) and between Figures 8(c) 505 and 10(a). For example, more inorganic species condense on particles in the fourth size section (between 0.0398 μm and 0.1585 μm) in the case of bulk equilibrium compared to the fully dynamic case. This section is dominated by CI 14 (HLI 33%, HBO 61%) (equal mixture of inorganic and hydrophobic organics) for bulk equilibrium, instead of CI 6 (HBO 81%) (unmixed hydrophobic organics) for dynamic. Internal and external distributions are similar with the dynamic approach, as 510 well as with the bulk equilibrium approach. Although internal and external compositions are different with the dynamic approach, they are quite similar with the bulk equilibrium approach. However, with the bulk equilibrium approach, similarly to the dynamic approach, unmixed particles of CI 3 (unmixed BC) remain present in most size sections for externally-mixed particles.

515 The mass and number distributions and compositions obtained with the hybrid approach are similar to the fully dynamic approach. For example, the over-condensation of inorganic species in the fourth size section (leading to particles of CI 14 (HLI 33%, HBO 61%) with bulk equilibrium) is restrained with the hybrid approach, as the fourth size section is computed dynamically, and particles consist of CI 6 (HBO 81%), as with the dynamic approach.

520 Table 3 shows the computational times (CPU) required for each simulation on a DELL Precision T3500 workstation (the lowest integration time step: 1). External mixing requires more CPU, especially for computing coagulation and dynamic C/E. The largest difference between internal and external mixing occurs for computing coagulation, which is almost 800 times slower with external mixing. Bulk equilibrium C/E provides a huge economy in CPU time for all simulations compared to dynamic C/E, while the computational advantage of hybrid C/E is more obvious for internal mixing (17 times faster than dynamic C/E) than external mixing (15% faster than dynamic C/E). This 525 significant speed degradation of the hybrid C/E scheme in the external mixing case is probably a consequence of small time steps used in the ROS2 solver because of the redistribution among the different composition sections performed after each time step. In other words, it takes CPU time to compute the dynamic distribution among the different composition sections.

530 **5 Conclusions**

A new Size-Composition Resolved Aerosol Model (SCRAM) has been developed to simulate the dynamic evolution of externally-mixed particles due to coagulation, condensation/evaporation, and nucleation. The general dynamic equation is discretised for both size and composition. Particle compositions are represented by the combinations of mass fractions, which may be chosen to correspond 535 either to the mass fraction of the different species or to the mass fraction of groups of species (e.g. inorganic, hydrophobic organics...). The total numbers and bounds of the size and composition sections are defined by the user. An automatic classification method is designed within the system to determine all the possible particle compositions based on the combinations of user-defined chemical species or groups and their mass-fraction sections.

540 The model was first validated by comparison to internally-mixed simulations of condensation / evaporation of sulphuric acid and of condensation / evaporation of sulphuric acid with coagulation. It was also validated for condensation against a reference solution.

The model was applied using realistic concentrations and typical emissions of air pollution over 545 Greater Paris, where traffic emissions are high. Initial concentrations were assumed to be internally mixed. Simulations lasted 12 h.

Although internally- and externally-mixed simulations lead to similar particle size distributions, the particle compositions are different. The externally-mixed simulations offer more details about particle mixing states within each size section when compared to internally mixed simulations. After 12 h, 49% of number concentrations and 24% of mass concentrations are not mixed. These percentages 550 may be higher in 3D simulations, because initial aerosol concentrations should not be assumed as entirely internally mixed over an urban area. Coagulation is quite efficient at mixing particles, as 52% of number concentrations and 36% of mass concentrations are not mixed if coagulation is not taken into account in the simulation. On the opposite, condensation may decrease the percentage of mixed particles when low-volatility gaseous emissions are high.

555 Assuming bulk equilibrium when solving condensation/evaporation leads to different distributions and compositions than the dynamic approach under both the internally- and externally-mixed assumptions. Although internally- and externally-mixed assumptions lead to similar compositions with the bulk equilibrium approach, unmixed particles remain when particles are externally mixed, as observed with the dynamic approach.

560 Although the simulation of externally mixed particles increases the computational cost, SCRAM offers the possibility to investigate particle mixing state in a comprehensive manner. Besides, its mixing state representation is flexible enough to be modified by users. Better computational performance could be reached with fewer, yet appropriately specified species groups and more optimised composition discretisations. For example, about half of the 20 compositions designed in this work 565 have really low mass concentrations (e.g. see Figures 7, 8, 9 and 10). Those compositions might be

dynamically deactivated in the future version of SCRAM to lower computational cost by using an algorithm to skip empty sections during coagulation and C/E processing.

Future work will focus on the optimisation and incorporation of SCRAM into the air quality modelling platform Polyphemus for 3D simulations. In order to investigate its performance in modelling air quality over Greater Paris, model simulation results will be compared to observations (Healy et al., 2012).

Code availability

The SCRAM source code related to this article is available under the URL: <http://cerea.enpc.fr/polyphemus/src/scram-1.0.tar.gz>, as a supplement package together with Read Me file, where hardware and software requirements, source code files and model output files are fully described.

SCRAM is a free software. You can redistribute it and/or modify it under the terms of the GNU General Public License as published by the Free Software Foundation.

Appendix A: Change of variables for the evolution of number and mass distributions

This appendix describes how to derive the equations of change for the number concentration \bar{n} and mass concentration \bar{q} distributions as a function of the variables $f_1, \dots, f_{(c-1)}, m$ used in the external mixing formulation.

To derive the equation of change for $\bar{n}(f_1, \dots, f_{(c-1)}, m)$ (Equation 5) from the equation of change for $n(m_1, \dots, m_c)$ (Equation 1), we need to perform a change of variables from m_1, \dots, m_c to $f_1, \dots, f_{(c-1)}, m$ and to compute the $[c \times c]$ Jacobian Matrix $\mathbf{J}(f_1, f_2, \dots, f_{(c-1)}, m)$

$$\mathbf{J} = \begin{bmatrix} \frac{\partial m_1}{\partial f_1} & \frac{\partial m_1}{\partial f_2} & \dots & \frac{\partial m_1}{\partial f_{(c-1)}} & \frac{\partial m_1}{\partial m} \\ \frac{\partial m_2}{\partial f_1} & \frac{\partial m_2}{\partial f_2} & \dots & \frac{\partial m_2}{\partial f_{(c-1)}} & \frac{\partial m_2}{\partial m} \\ \vdots & \vdots & \ddots & \vdots & \vdots \\ \frac{\partial m_{(c-1)}}{\partial f_1} & \frac{\partial m_{(c-1)}}{\partial f_2} & \dots & \frac{\partial m_{(c-1)}}{\partial f_{(c-1)}} & \frac{\partial m_{(c-1)}}{\partial m} \\ \frac{\partial m_c}{\partial f_1} & \frac{\partial m_c}{\partial f_2} & \dots & \frac{\partial m_c}{\partial f_{(c-1)}} & \frac{\partial m_c}{\partial m} \end{bmatrix}$$

(A1)

$$585 = \begin{bmatrix} m & 0 & \dots & 0 & f_1 \\ 0 & m & \dots & 0 & f_2 \\ \vdots & \vdots & \ddots & \vdots & \vdots \\ 0 & 0 & \dots & m & f_{(c-1)} \\ -m & -m & \dots & -m & 1 - \sum_{i=1}^{(c-1)} f_i \end{bmatrix}$$

and the Jacobian inverse matrix:

$$\mathbf{J}^{-1} = \begin{bmatrix} \frac{1-f_1}{m} & -\frac{f_1}{m} & \dots & -\frac{f_1}{m} & -\frac{f_1}{m} \\ -\frac{f_2}{m} & \frac{1-f_2}{m} & \dots & -\frac{f_2}{m} & -\frac{f_2}{m} \\ \vdots & \vdots & \ddots & \vdots & \vdots \\ -\frac{f_{(c-1)}}{m} & -\frac{f_{(c-1)}}{m} & \dots & \frac{1-f_{(c-1)}}{m} & -\frac{f_{(c-1)}}{m} \\ 1 & 1 & \dots & 1 & 1 \end{bmatrix} \quad (\text{A2})$$

The relationship between n and \bar{n} is

$$n = \frac{\bar{n}}{\det(J)} = \frac{\bar{n}}{m^{(c-1)}} \quad (\text{A3})$$

590 Thus,

$$\frac{\partial n}{\partial t} = \frac{\partial(\frac{\bar{n}}{m^{(c-1)}})}{\partial t} = \frac{1}{m^{(c-1)}} \frac{\partial \bar{n}}{\partial t} \quad (\text{A4})$$

For the right-hand side of Equation (1), the terms $\frac{\partial(I_i n)}{\partial m_i}$ are replaced by terms depending on the new variables, using:

$$\left(\frac{\partial(I_1 n)}{\partial m_1}, \frac{\partial(I_2 n)}{\partial m_2}, \dots, \frac{\partial(I_c n)}{\partial m_c} \right) = \left(\frac{\partial(I_1 n)}{\partial f_1}, \frac{\partial(I_2 n)}{\partial f_2}, \dots, \frac{\partial(I_{c-1} n)}{\partial f_{c-1}}, \frac{\partial(I_c n)}{\partial m} \right) \times \mathbf{J}^{-1} \quad (\text{A5})$$

595 For $i \in (1, (c-1))$, this leads to:

$$\frac{\partial(I_i n)}{\partial m_i} = \frac{1}{m} \frac{\partial(I_i n)}{\partial f_i} - \sum_{j=1}^{(c-1)} \frac{f_j}{m} \frac{\partial(I_i n)}{\partial f_j} + \frac{\partial(I_i n)}{\partial m} \quad (\text{A6})$$

and for $i = c$:

$$\frac{\partial(I_c n)}{\partial m_c} = - \sum_{j=1}^{(c-1)} \frac{f_j}{m} \frac{\partial(I_c n)}{\partial f_j} + \frac{\partial(I_c n)}{\partial m} \quad (\text{A7})$$

If we replace I_c with $I_0 - \sum_{i=1}^{(c-1)} I_i$ in (A7), we have:

$$600 \quad \frac{\partial(I_c n)}{\partial m_c} = - \sum_{j=1}^{(c-1)} \frac{f_j}{m} \frac{\partial(I_0 n)}{\partial f_j} + \sum_{i=1}^{(c-1)} \sum_{j=1}^{(c-1)} \frac{f_j}{m} \frac{\partial(I_i n)}{\partial f_j} + \frac{\partial(I_0 n)}{\partial m} - \sum_{i=1}^{(c-1)} \frac{\partial(I_i n)}{\partial m} \quad (\text{A8})$$

The sum of the first $(c-1)$ terms of the right side of Equation (1) may be written as follows.

$$\sum_{i=1}^{(c-1)} \frac{\partial(I_i n)}{\partial m_i} = \frac{1}{m} \sum_{i=1}^{(c-1)} \frac{\partial(I_i n)}{\partial f_i} - \sum_{i=1}^{(c-1)} \sum_{j=1}^{(c-1)} \frac{f_j}{m} \frac{\partial(I_i n)}{\partial f_j} + \sum_{i=1}^{(c-1)} \frac{\partial(I_i n)}{\partial m} \quad (\text{A9})$$

The right-hand side of Equation (1) becomes

$$-\sum_{i=1}^c \frac{\partial(I_i n)}{\partial m_i} = - \sum_{i=1}^{(c-1)} \frac{\partial(I_i n)}{\partial m_i} - \frac{\partial(I_c n)}{\partial m_c} = -\frac{1}{m} \sum_{i=1}^{(c-1)} \frac{\partial(I_i n)}{\partial f_i} + \sum_{i=1}^{(c-1)} \frac{f_i}{m} \frac{\partial(I_0 n)}{\partial f_i} - \frac{\partial(I_0 n)}{\partial m}$$

(A10)

605 If we denote $H_i = \frac{\partial f_i}{\partial t}$, then I_i may be written as follows.

$$I_i = \frac{\partial m_i}{\partial t} = \frac{\partial(m f_i)}{\partial t} = m \frac{\partial f_i}{\partial t} + f_i \frac{\partial m}{\partial t} = m H_i + f_i I_0 \quad (\text{A11})$$

Replacing I_i by (A11) in (A10) and using $\frac{\partial m}{\partial f_i} = 0$,

$$\begin{aligned} -\sum_{i=1}^c \frac{\partial(I_i n)}{\partial m_i} &= -\frac{1}{m} \sum_{i=1}^{(c-1)} \frac{\partial(m H_i n + f_i I_0 n)}{\partial f_i} + \sum_{i=1}^{(c-1)} \frac{f_i}{m} \frac{\partial(I_0 n)}{\partial f_i} - \frac{\partial(I_0 n)}{\partial m} \\ &= -\sum_{i=1}^{(c-1)} \frac{\partial(H_i n)}{\partial f_i} - \frac{(c-1)}{m} I_0 n - \frac{\partial(I_0 n)}{\partial m} \end{aligned} \quad (\text{A12})$$

Replacing n with $\frac{\bar{n}}{m^{(c-1)}}$ in Equation (1) and using (A12), we have

$$\begin{aligned} \frac{1}{m^{(c-1)}} \frac{\partial \bar{n}}{\partial t} &= -\sum_{i=1}^{(c-1)} \frac{\partial(H_i \frac{\bar{n}}{m^{(c-1)}})}{\partial f_i} - \frac{(c-1)}{m^c} I_0 \bar{n} - \frac{\partial(I_0 \frac{\bar{n}}{m^{(c-1)}})}{\partial m} \\ &= -\frac{1}{m^{(c-1)}} \sum_{i=1}^{(c-1)} \frac{\partial(H_i \bar{n})}{\partial f_i} - \frac{1}{m^{(c-1)}} \frac{\partial(I_0 \bar{n})}{\partial m} \end{aligned} \quad (\text{A13})$$

and the equation of change for \bar{n} is finally

$$\frac{\partial \bar{n}}{\partial t} = -\sum_{i=1}^{(c-1)} \frac{\partial(H_i \bar{n})}{\partial f_i} - \frac{\partial(I_0 \bar{n})}{\partial m} \quad (\text{A14})$$

The equation of change for the mass distribution $q_i = n m_i$ of species i is derived as follows.

$$\frac{\partial q_i}{\partial t} = \frac{\partial n m_i}{\partial t} = -m_i \frac{\partial n}{\partial t} + n I_i \quad (\text{A15})$$

615 And the equation of change for \bar{q}_i is obtained using $n = \frac{\bar{n}}{m^{(c-1)}}$, $q_i = \frac{\bar{q}_i}{m^{(c-1)}}$ and $m_i = m f_i$

$$\frac{\partial \bar{q}_i}{\partial t} = -m f_i \frac{\partial \bar{n}}{\partial t} + \bar{n} I_i \quad (\text{A16})$$

Appendix B: The time derivation of Equation (10) and (9)

The time derivation of Equation (10) leads to:

$$\begin{aligned}
\frac{\partial N^j}{\partial t} = & \overbrace{\int_{m_k^- f_{g_1}^-}^{m_k^+ f_{g_1}^+} \dots \int_{f_{g_{(c-1)}}^-}^{f_{g_{(c-1)}}^+} \frac{\partial \bar{n}}{\partial t} dm df_{g_1}, \dots, df_{g_{(c-1)}}}^A \\
& + \overbrace{\frac{dm_k^+}{dt} \int_{f_{g_1}^-}^{f_{g_1}^+} \dots \int_{f_{g_{(c-1)}}^-}^{f_{g_{(c-1)}}^+} \bar{n}(m_k^+, f_{g_1}, \dots, f_{g_{(c-1)}}) df_{g_1}, \dots, df_{g_{(c-1)}} - \frac{dm_k^-}{dt} \int_{f_{g_1}^-}^{f_{g_1}^+} \dots \int_{f_{g_{(c-1)}}^-}^{f_{g_{(c-1)}}^+} \bar{n}(m_k^-, f_{g_1}, \dots, f_{g_{(c-1)}}) df_{g_1}, \dots, df_{g_{(c-1)}}}^B \\
& + \sum_{i=1}^{(c-1)} \left[\frac{df_{g_i}^+}{dt} \int_{m_k^- f_{g_1}^-}^{m_k^+ f_{g_1}^+} \dots \int_{f_{g_{i-1}}^- f_{g_{i+1}}^-}^{f_{g_{i-1}}^+ f_{g_{i+1}}^+} \dots \int_{f_{g_{(c-1)}}^-}^{f_{g_{(c-1)}}^+} \bar{n}(m, f_{g_1}, \dots, f_{g_{i-1}}, f_{g_i^+}, f_{g_{i+1}}, \dots, f_{g_{(c-1)}}) dm df_{g_1} \dots df_{g_{i-1}} df_{g_{i+1}} \dots df_{g_{(c-1)}} \right. \\
& \left. - \frac{df_{g_i}^-}{dt} \int_{m_k^- f_{g_1}^-}^{m_k^+ f_{g_1}^+} \dots \int_{f_{g_{i-1}}^- f_{g_{i+1}}^-}^{f_{g_{i-1}}^+ f_{g_{i+1}}^+} \dots \int_{f_{g_{(c-1)}}^-}^{f_{g_{(c-1)}}^+} \bar{n}(m, f_{g_1}, \dots, f_{g_{i-1}}, f_{g_i^-}, f_{g_{i+1}}, \dots, f_{g_{(c-1)}}) dm df_{g_1} \dots df_{g_{i-1}} df_{g_{i+1}} \dots df_{g_{(c-1)}} \right] \tag{B1}
\end{aligned}$$

620 Replacing $\frac{\partial \bar{n}}{\partial t}(m, f_{g_1}, \dots, f_{g_{(c-1)}})$ by Equation (5), we have

$$A = \int_{m_k^- f_{g_1}^-}^{m_k^+ f_{g_1}^+} \dots \int_{f_{g_{(c-1)}}^-}^{f_{g_{(c-1)}}^+} \left[-\frac{\partial(I_0 n)}{\partial m} - \sum_{x=1}^{(c-1)} \frac{\partial(H_{g_x} n)}{\partial f_{g_x}} \right] dm df_{g_1} \dots df_{g_{(c-1)}} \tag{B2}$$

and using $I_0 = \frac{dm}{dt}$, $H_{g_i} = \frac{df_{g_i}}{dt}$ and $\frac{\partial f_{g_i}}{\partial f_{g_l}} = 0$ when $i \neq l$

$$\begin{aligned}
A = & - \left\{ \frac{dm_k^+}{dt} \int_{f_{g_1}^-}^{f_{g_1}^+} \dots \int_{f_{g_{(c-1)}}^-}^{f_{g_{(c-1)}}^+} \bar{n}(m_k^+, f_{g_1}, \dots, f_{g_{(c-1)}}) dm df_{g_1} \dots df_{g_{(c-1)}} - \frac{dm_k^-}{dt} \int_{f_{g_1}^-}^{f_{g_1}^+} \dots \int_{f_{g_{(c-1)}}^-}^{f_{g_{(c-1)}}^+} \bar{n}(m_k^-, f_{g_1}, \dots, f_{g_{(c-1)}}) dm df_{g_1} \dots df_{g_{(c-1)}} \right. \\
& + \sum_{i=1}^{(c-1)} \left[\frac{df_{g_i}^+}{dt} \int_{m_k^- f_{g_1}^-}^{m_k^+ f_{g_1}^+} \dots \int_{f_{g_{i-1}}^- f_{g_{i+1}}^-}^{f_{g_{i-1}}^+ f_{g_{i+1}}^+} \dots \int_{f_{g_{(c-1)}}^-}^{f_{g_{(c-1)}}^+} \bar{n}(m, f_{g_1}, \dots, f_{g_{i-1}}, f_{g_i^+}, f_{g_{i+1}}, \dots, f_{g_{(c-1)}}) dm df_{g_1} \dots df_{g_{i-1}} df_{g_{i+1}} \dots df_{g_{(c-1)}} \right. \\
& \left. - \frac{df_{g_i}^-}{dt} \int_{m_k^- f_{g_1}^-}^{m_k^+ f_{g_1}^+} \dots \int_{f_{g_{i-1}}^- f_{g_{i+1}}^-}^{f_{g_{i-1}}^+ f_{g_{i+1}}^+} \dots \int_{f_{g_{(c-1)}}^-}^{f_{g_{(c-1)}}^+} \bar{n}(m, f_{g_1}, \dots, f_{g_{i-1}}, f_{g_i^-}, f_{g_{i+1}}, \dots, f_{g_{(c-1)}}) dm df_{g_1} \dots df_{g_{i-1}} df_{g_{i+1}} \dots df_{g_{(c-1)}} \right] \right\} \tag{B3}
\end{aligned}$$

So $A = -B$, thus

$$625 \quad \frac{\partial N^j}{\partial t} = (A + B) = 0 \quad (\text{B4})$$

which is expected since condensation/evaporation does not affect the total number of particles.

Similarly, an equation of change can be derived for Q_i^j . In order to simplify the writing of the equations, the following abbreviations are introduced:

$$\begin{aligned} f_{g_1^{(c-1)}} &= f_{g_1}, \dots, f_{g_{(c-1)}} \\ f_{g_1^{(c-1)} \setminus i} &= f_{g_1}, \dots, f_{g_{i-1}}, f_{g_{i+1}}, \dots, f_{g_{(c-1)}} \\ df_{g_1^{(c-1)}} &= df_{g_1} \dots df_{g_{(c-1)}} \\ df_{g_1^{(c-1)} \setminus i} &= df_{g_1} \dots df_{g_{i-1}} df_{g_{i+1}} \dots df_{g_{(c-1)}} \\ \int_{f_{g_1^{(c-1)}}}^{f_{g_1^{(c-1)}}} &= \int_{f_{g_1}}^{f_{g_1}} \dots \int_{f_{g_{(c-1)}}}^{f_{g_{(c-1)}}} \\ \int_{f_{g_1^{(c-1)} \setminus i}}^{f_{g_1^{(c-1)} \setminus i}} &= \int_{f_{g_1}}^{f_{g_1}} \dots \int_{f_{g_{i-1}}}^{f_{g_{i-1}}} \int_{f_{g_{i+1}}}^{f_{g_{i+1}}} \dots \int_{f_{g_{(c-1)}}}^{f_{g_{(c-1)}}} \\ f_{g_1^{(c-1)} \setminus i} &= f_{g_1} \dots f_{g_{i-1}} f_{g_{i+1}} \dots f_{g_{(c-1)}} \end{aligned}$$

630 The time derivation of Equation (9) leads to:

$$\begin{aligned} \frac{\partial Q_i^j}{\partial t} &= \int_{m_k^- f_{g_1^{(c-1)}}^-}^{m_k^+ f_{g_1^{(c-1)}}^+} \int_{f_{g_1^{(c-1)}}}^{f_{g_1^{(c-1)}}} \frac{\partial \bar{q}_i}{\partial t} dm df_{g_1^{(c-1)}} \\ &+ \frac{dm_k^+}{dt} \int_{f_{g_1^{(c-1)}}^-}^{f_{g_1^{(c-1)}}^+} \bar{q}_i(m_k^+, f_{g_1^{(c-1)}}) df_{g_1^{(c-1)}} - \frac{dm_k^-}{dt} \int_{f_{g_1^{(c-1)}}^-}^{f_{g_1^{(c-1)}}^+} \bar{q}_i(m_k^-, f_{g_1^{(c-1)}}) df_{g_1^{(c-1)}} \\ &+ \sum_{i=1}^{(c-1)} \left[\frac{df_{g_1^{(c-1)}}^+}{dt} \int_{m_k^- f_{g_1^{(c-1)} \setminus i}^-}^{m_k^+ f_{g_1^{(c-1)} \setminus i}^+} \int_{f_{g_1^{(c-1)} \setminus i}}^{f_{g_1^{(c-1)} \setminus i}} \bar{q}_i(m, f_{g_i}^+, f_{g_1^{(c-1)} \setminus i}) dm df_{g_1^{(c-1)} \setminus i} \right. \\ &\quad \left. - \frac{df_{g_1^{(c-1)}}^-}{dt} \int_{m_k^- f_{g_1^{(c-1)} \setminus i}^-}^{m_k^+ f_{g_1^{(c-1)} \setminus i}^+} \int_{f_{g_1^{(c-1)} \setminus i}}^{f_{g_1^{(c-1)} \setminus i}} \bar{q}_i(m, f_{g_i}^-, f_{g_1^{(c-1)} \setminus i}) dm df_{g_1^{(c-1)} \setminus i} \right] \end{aligned} \quad (\text{B5})$$

Substituting Equation (A16) and $\bar{q}_i = m f_i \bar{n}$ into Equation (B5), we obtain:

$$\begin{aligned}
\frac{\partial Q_i^j}{\partial t} = & \overbrace{\int_{m_k^- f_{g_1^{(c-1)}}}^{m_k^+ f_{g_1^{(c-1)}}} \int m f_{g_i} \frac{\partial \bar{n}}{\partial t} dm df_{g_1^{(c-1)}} + \int_{m_k^- f_{g_1^{(c-1)}}}^{m_k^+ f_{g_1^{(c-1)}}} \bar{n} I_{g_i} dm df_{g_1^{(c-1)}}}^C \\
& + \overbrace{m_k^+ \frac{dm_k^+}{dt} \int_{f_{g_1^{(c-1)}}}^{f_{g_1^{(c-1)}}} f_{g_i} \bar{n}(m_k^+, f_{g_1^{(c-1)}}) df_{g_1^{(c-1)}} - m_k^- \frac{dm_k^-}{dt} \int_{f_{g_1^{(c-1)}}}^{f_{g_1^{(c-1)}}} f_{g_i} \bar{n}(m_k^-, f_{g_1^{(c-1)}}) df_{g_1^{(c-1)}}}^D \\
& + \sum_{i=1}^{(c-1)} \left[f_{g_i}^+ \frac{df_{g_1^{(c-1)}}^+}{dt} \int_{m_k^- f_{g_1^{(c-1)} \setminus i}}^{m_k^+ f_{g_1^{(c-1)} \setminus i}} m \bar{n}(m, f_{g_i}^+, f_{g_1^{(c-1)} \setminus i}) dm df_{g_1^{(c-1)} \setminus i} \right. \\
& \quad \left. - f_{g_i}^- \frac{df_{g_1^{(c-1)}}^-}{dt} \int_{m_k^- f_{g_1^{(c-1)} \setminus i}}^{m_k^+ f_{g_1^{(c-1)} \setminus i}} m \bar{n}(m, f_{g_i}^-, f_{g_1^{(c-1)} \setminus i}) dm df_{g_1^{(c-1)} \setminus i} \right]
\end{aligned} \tag{B6}$$

Similarly to Equation (B1), it can be proved that $C = -D$, so that Equation (B6) simplifies to:

$$635 \quad \frac{\partial Q_i^j}{\partial t} = \int_{m_k^- f_{g_1^{(c-1)}}}^{m_k^+ f_{g_1^{(c-1)}}} \bar{n} I_{g_i} dm df_{g_1^{(c-1)}} = N^j I_{g_i} \tag{B7}$$

Thus, in each section, the change with time of number and mass concentrations is given by Equations (B4) and (B7).

Acknowledgements. The authors gratefully acknowledge Hilel Dergaoui (INRA) for providing his original code of coagulation process and Edouard Debry (INERIS) for optimising the computation of coagulation distribution coefficients. We also would like to thank Florian Couvidat (INERIS) for his support on the implementation of his H²O model into SCRAM as well as Stéphanie Deschamps (CEREA) who helped to improve the size redistribution algorithm.

References

Bauer, S., Wright, D., Koch, D., Lewis, E., McGraw, R., Chang, L.-S., Schwartz, S., and Ruedy, R.: MATRIX
645 (Multiconfiguration Aerosol TRacker of mIXing state): an aerosol microphysical module for global atmospheric models, *Atmospheric Chemistry and Physics*, 8, 6003–6035, 2008.

Binkowski, F. S. and Roselle, S. J.: Models-3 Community Multiscale Air Quality (CMAQ) model aerosol component 1. Model description, *Journal of Geophysical Research: Atmospheres* (1984–2012), 108, 2003.

Capaldo, K., Pilinis, C., and Pandis, S. N.: A computationally efficient hybrid approach for dynamic gas/aerosol
650 transfer in air quality models, *Atmospheric Environment*, 34, 3617–3627, 2000.

Couvidat, F., Debry, É., Sartelet, K., and Seigneur, C.: A hydrophilic/hydrophobic organic (H₂O) aerosol model: Development, evaluation and sensitivity analysis, *Journal of Geophysical Research: Atmospheres* (1984–2012), 117, 2012.

Couvidat, F., Kim, Y., Sartelet, K., Seigneur, C., Marchand, N., and Sciare, J.: Modeling secondary organic
655 aerosol in an urban area: application to Paris, France, *Atmospheric Chemistry and Physics*, 13, 983–996, 2013.

Dahneke, B.: Simple kinetic theory of Brownian diffusion in vapors and aerosols, in: *Theory of Dispersed Multiphase Flow*, pp. 97–133, Academic Press, 1983.

Deboudt, K., Flament, P., Choël, M., Gloter, A., Sobanska, S., and Colliex, C.: Mixing state of aerosols and
660 direct observation of carbonaceous and marine coatings on African dust by individual particle analysis, *Journal of Geophysical Research: Atmospheres* (1984–2012), 115, 2010.

Debry, E. and Sportisse, B.: Reduction of the condensation/evaporation dynamics for atmospheric aerosols: Theoretical and numerical investigation of hybrid methods, *Journal of Aerosol Science*, 37, 950–966, 2006.

Debry, E., Fahey, K., Sartelet, K., Sportisse, B., and Tombette, M.: Technical Note: A new SIZe REsolved
665 Aerosol Model (SIREAM), *Atmospheric Chemistry and Physics*, 7, 1537–1547, 2007.

Dergaoui, H., Sartelet, K. N., Debry, É., and Seigneur, C.: Modeling coagulation of externally mixed particles: Sectional approach for both size and chemical composition, *Journal of Aerosol Science*, 58, 17 – 32, 2013.

Devilliers, M., Debry, É., Sartelet, K., and Seigneur, C.: A new algorithm to solve condensation/evaporation for ultra fine, fine, and coarse particles, *Journal of Aerosol Science*, 55, 116–136, 2013.

Djouad, R., Sportisse, B., and Audiffren, N.: Numerical simulation of aqueous-phase atmospheric models: use
670 of a non-autonomous Rosenbrock method, *Atmospheric Environment*, 36, 873–879, 2002.

EPA, D.: Integrated science assessment for particulate matter, US Environmental Protection Agency Washington, DC, 2009.

Gelbard, F. and Seinfeld, J. H.: Simulation of multicomponent aerosol dynamics, *Journal of colloid and Interface
675 Science*, 78, 485–501, 1980.

Healy, R., Sciare, J., Poulain, L., Kamili, K., Merkel, M., Müller, T., Wiedensohler, A., Eckhardt, S., Stohl, A.,
Sarda-Estève, R., et al.: Sources and mixing state of size-resolved elemental carbon particles in a European
megacity: Paris, *Atmospheric Chemistry and Physics*, 12, 1681–1700, 2012.

Hughes, L. S., Allen, J. O., Bhave, P., Kleeman, M. J., Cass, G. R., Liu, D.-Y., Fergenson, D. P., Morrical,
680 B. D., and Prather, K. A.: Evolution of atmospheric particles along trajectories crossing the Los Angeles
basin, *Environmental science & technology*, 34, 3058–3068, 2000.

Jacobson, M.: Analysis of aerosol interactions with numerical techniques for solving coagulation, nucleation, condensation, dissolution, and reversible chemistry among multiple size distributions, *Journal of Geophysical Research*, 107, 1327–1338, 2002.

685 Jacobson, M. Z.: Development and application of a new air pollution modeling system—II. Aerosol module structure and design, *Atmospheric Environment*, 31, 131–144, 1997.

Jacobson, M. Z.: Strong radiative heating due to the mixing state of black carbon in atmospheric aerosols, *Nature*, 409, 695–697, 2001.

Jacobson, M. Z., Turco, R. P., Jensen, E. J., and Toon, O. B.: Modeling coagulation among particles of different 690 composition and size, *Atmospheric Environment*, 28, 1327–1338, 1994.

Kleeman, M. J. and Cass, G. R.: A 3D Eulerian source-oriented model for an externally mixed aerosol, *Environmental science & technology*, 35, 4834–4848, 2001.

Kleeman, M. J., Cass, G. R., and Eldering, A.: Modeling the airborne particle complex as a source-oriented external mixture, *Journal of Geophysical Research: Atmospheres (1984–2012)*, 102, 21 355–21 372, 1997.

695 Leck, N. and Svensson, E.: Importance of aerosol composition and mixing state for cloud droplet activation in the high Arctic, *Atmospheric Chemistry and Physics Discussion*, 14, 21 223–21 283, 2014.

Lesins, G., Chylek, P., and Lohmann, U.: A study of internal and external mixing scenarios and its effect on aerosol optical properties and direct radiative forcing, *Journal of Geophysical Research: Atmospheres (1984–2012)*, 107, AAC–5, 2002.

700 Lu, J. and Bowman, F. M.: A detailed aerosol mixing state model for investigating interactions between mixing state, semivolatile partitioning, and coagulation, *Atmospheric Chemistry and Physics*, 10, 4033–4046, 2010.

Mallet, M., Roger, J., Despiau, S., Putaud, J., and Dubovik, O.: A study of the mixing state of black carbon in urban zone, *Journal of Geophysical Research: Atmospheres (1984–2012)*, 109, 2004.

McMurtry, P. H.: A review of atmospheric aerosol measurements, *Atmospheric Environment*, 34, 1959–1999, 705 2000.

Myhre, G., Samset, B., Schulz, M., Balkanski, Y., Bauer, S., Berntsen, T., Bian, H., Bellouin, N., Chin, M., Diehl, T., et al.: Radiative forcing of the direct aerosol effect from AeroCom Phase II simulations, *Atmospheric Chemistry and Physics*, 13, 1853–1877, 2013.

Nenes, A., Pandis, S. N., and Pilinis, C.: ISORROPIA: A new thermodynamic equilibrium model for multiphase 710 multicomponent inorganic aerosols, *Aquatic geochemistry*, 4, 123–152, 1998.

Oshima, N., Koike, M., Zhang, Y., Kondo, Y., Moteki, N., Takegawa, N., and Miyazaki, Y.: Aging of black carbon in outflow from anthropogenic sources using a mixing state resolved model: Model development and evaluation, *Journal of Geophysical Research: Atmospheres (1984–2012)*, 114, 2009.

Pandis, S. N., Wexler, A. S., and Seinfeld, J. H.: Secondary organic aerosol formation and transport—II. Predicting the ambient secondary organic aerosol size distribution, *Atmospheric Environment. Part A. General Topics*, 27, 2403–2416, 1993.

Pascal, M., Corso, M., Chanel, O., Declercq, C., Badaloni, C., Cesaroni, G., Henschel, S., Meister, K., Haluza, D., Martin-Olmedo, P., et al.: Assessing the public health impacts of urban air pollution in 25 European cities: Results of the Aphekom project, *Science of the Total Environment*, 449, 390–400, 2013.

720 Pilinis, C., Capaldo, K., Nenes, A., and Pandis, S.: MADM-A new multicomponent aerosol dynamics model, *Aerosol Science & Technology*, 32, 482–502, 2000.

Riemer, N., West, M., Zaveri, R. A., and Easter, R. C.: Simulating the evolution of soot mixing state with a particle-resolved aerosol model, *Journal of Geophysical Research*, 114, D09202, 2009.

Sartelet, K., Debry, E., Fahey, K., Roustan, Y., Tombette, M., and Sportisse, B.: Simulation of aerosols and 725 gas-phase species over Europe with the Polyphemus system: Part I Model-to-data comparison for 2001, *Atmospheric Environment*, 41, 6116–6131, 2007.

Seigneur, C., Hudischewskyj, a. B., Seinfeld, J. H., Whitby, K. T., Whitby, E. R., Brock, J. R., and Barnes, H. M.: Simulation of Aerosol Dynamics: A Comparative Review of Mathematical Models, *Aerosol Science and Technology*, 5, 205–222, 1986.

730 Stier, P., Feichter, J., Kinne, S., Kloster, S., Vignati, E., Wilson, J., Ganzeveld, L., Tegen, I., Werner, M., Balkanski, Y., et al.: The aerosol-climate model ECHAM5-HAM, *Atmospheric Chemistry and Physics*, 5, 1125–1156, 2005.

Vehkamäki, H., Kulmala, M., Napari, I., Lehtinen, K. E., Timmreck, C., Noppel, M., and Laaksonen, A.: An 735 improved parameterization for sulfuric acid–water nucleation rates for tropospheric and stratospheric conditions, *Journal of Geophysical Research: Atmospheres* (1984–2012), 107, AAC–3, 2002.

Verwer, J. G., Spee, E., Blom, J., and Hundsdorfer, W.: A second-order Rosenbrock method applied to photochemical dispersion problems, *SIAM Journal on Scientific Computing*, 20, 1456–1480, 1999.

Wexler, A. S. and Seinfeld, J. H.: The distribution of ammonium salts among a size and composition dispersed aerosol, *Atmospheric Environment. Part A. General Topics*, 24, 1231–1246, 1990.

740 Whitby, E. R. and McMurry, P. H.: Modal aerosol dynamics modeling, *Aerosol Science and Technology*, 27, 673–688, 1997.

Zhang, Y., Seigneur, C., Seinfeld, J. H., Jacobson, M. Z., and Binkowski, F. S.: Simulation of Aerosol Dynamics: A Comparative Review of Algorithms Used in Air Quality Models, *Aerosol Science and Technology*, 31, 487–514, 1999.

745 Zhang, Y., Pun, B., Vijayaraghavan, K., Wu, S.-Y., Seigneur, C., Pandis, S. N., Jacobson, M. Z., Nenes, A., and Seinfeld, J. H.: Development and application of the model of aerosol dynamics, reaction, ionization, and dissolution (MADRID), *Journal of Geophysical Research: Atmospheres* (1984–2012), 109, 2004.

Zhang, Y., McMurry, P. H., Yu, F., and Jacobson, M. Z.: A comparative study of nucleation parameterizations: 750 1. Examination and evaluation of the formulations, *Journal of Geophysical Research: Atmospheres* (1984–2012), 115, 2010.

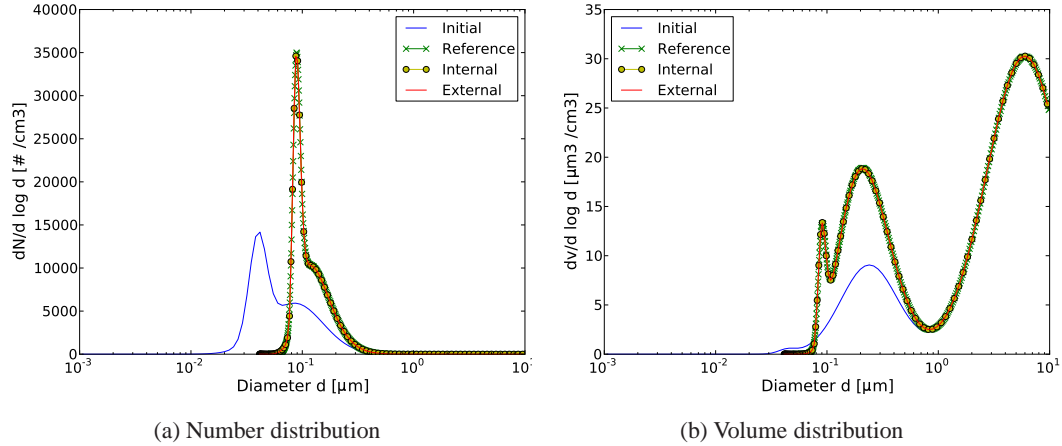


Figure 1. Simulation of condensation for hazy conditions: initial distribution and after 12 hours.

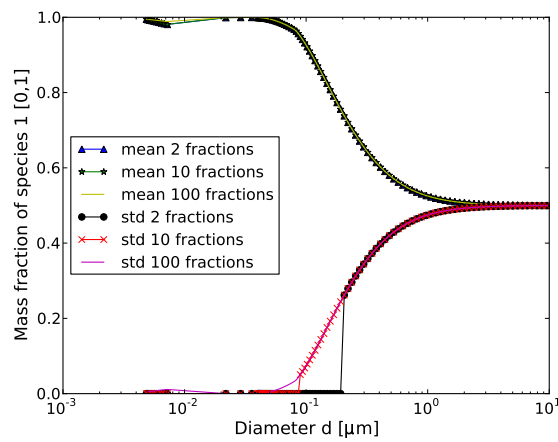


Figure 2. Mean and standard deviations of species 1 mass fraction as functions of particle diameter using 2, 10 and 100 composition sections.

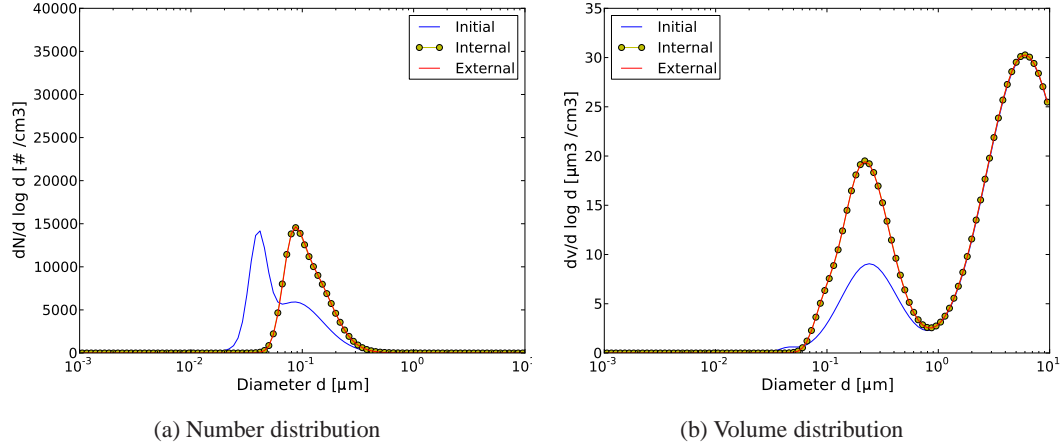


Figure 3. Simulation of both coagulation and condensation for hazy conditions: initial distribution and after 12 hours.

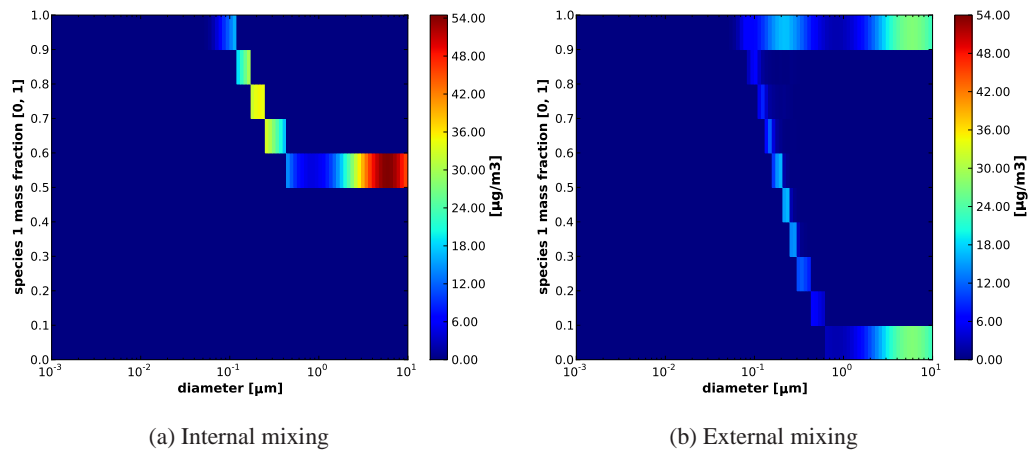


Figure 4. Distribution after 12 hours: particle mass concentration as a function of diameter and mass fraction of species 1.

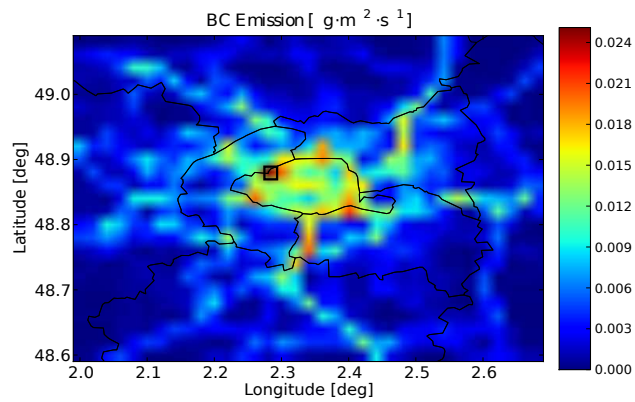


Figure 5. BC emissions over Greater Paris at 2 UT, 1 July 2009.

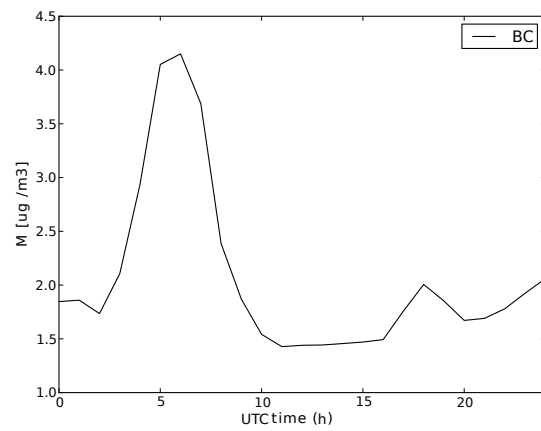


Figure 6. Transprt BC concentrations profile of on 1 July 2009.

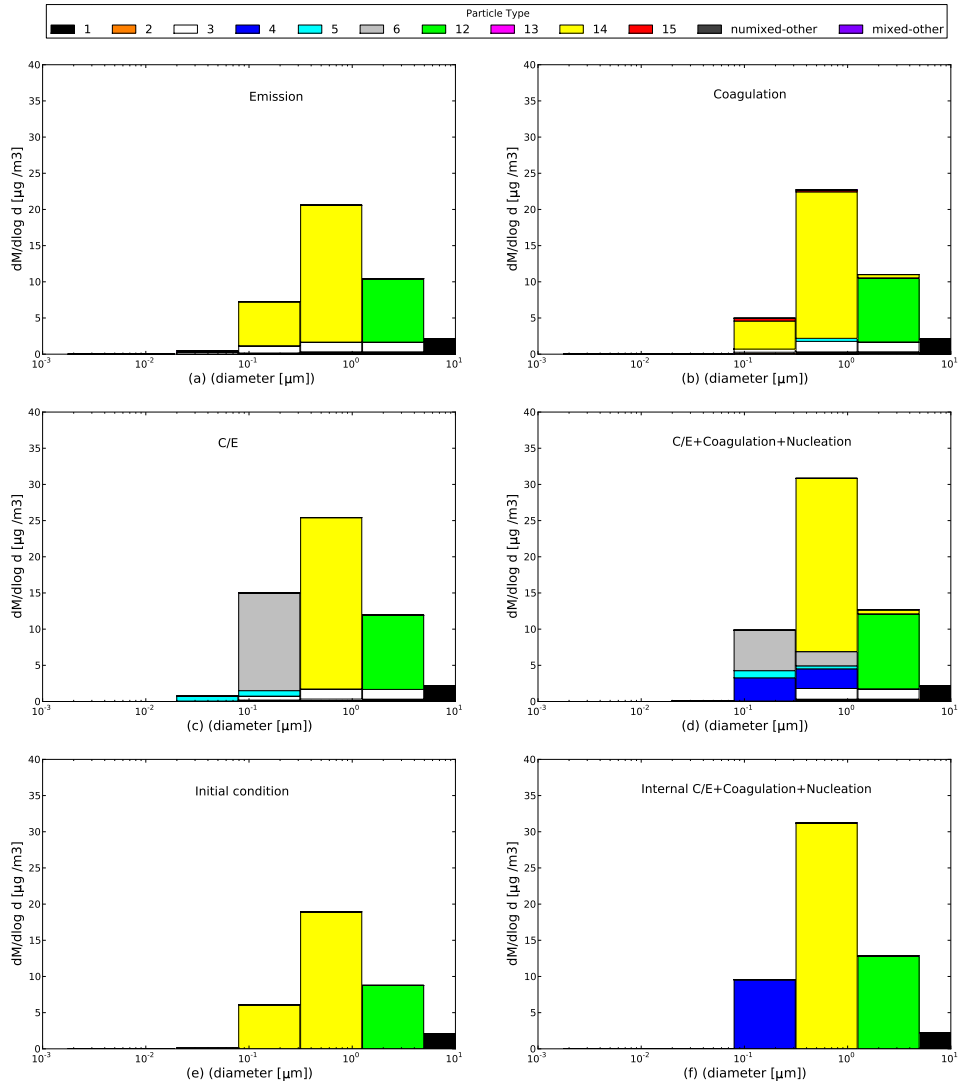


Figure 7. Result mass distributions of externally-mixed particles as a function of particle diameter for the different chemical compositions for 6 different simulation scenarios: (a) Emission only; (b) Emission+Coagulation; (c) Emission+C/E; (d) Emission+Coagulation+C/E+nucleation; (e) Initial Condition; (f) Internal mixing result.

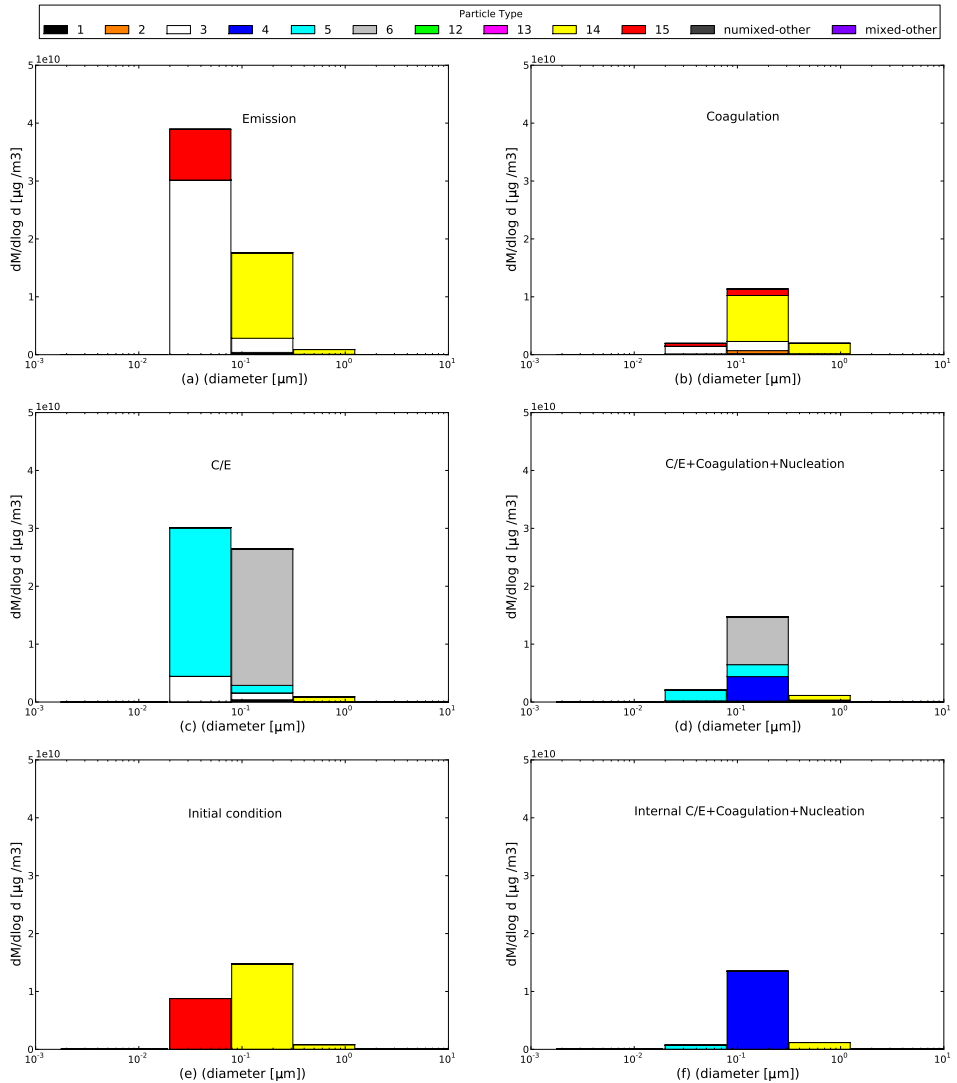


Figure 8. Result number distributions of externally-mixed particles as a function of particle diameter for the different chemical compositions for 6 different simulation scenarios: (a) Emission only; (b) Emission+Coagulation; (c) Emission+C/E; (d) Emission+Coagulation+C/E+nucleation; (e) Initial Condition; (f) Internal mixing result.

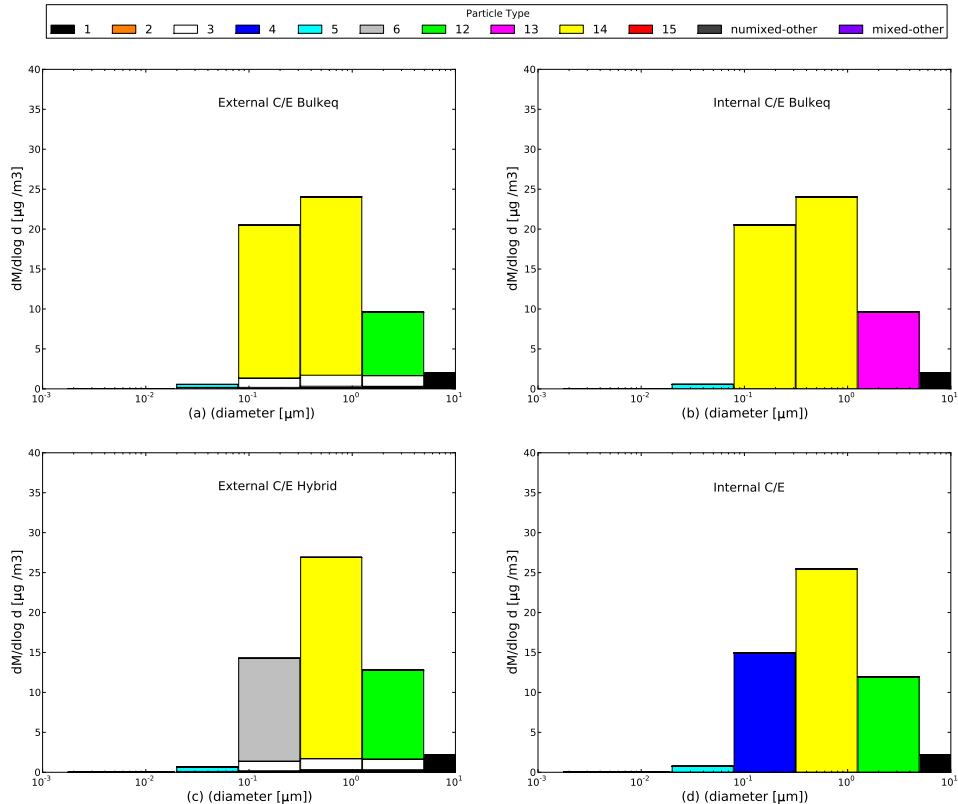


Figure 9. Result mass distributions of externally-mixed particles as a function of particle diameter for the different chemical compositions for 4 different C/E simulation scenarios: (a) External bulk-equilibrium; (b) Internal bulk-equilibrium; (c) External hybrid method; (d) Internal dynamic.

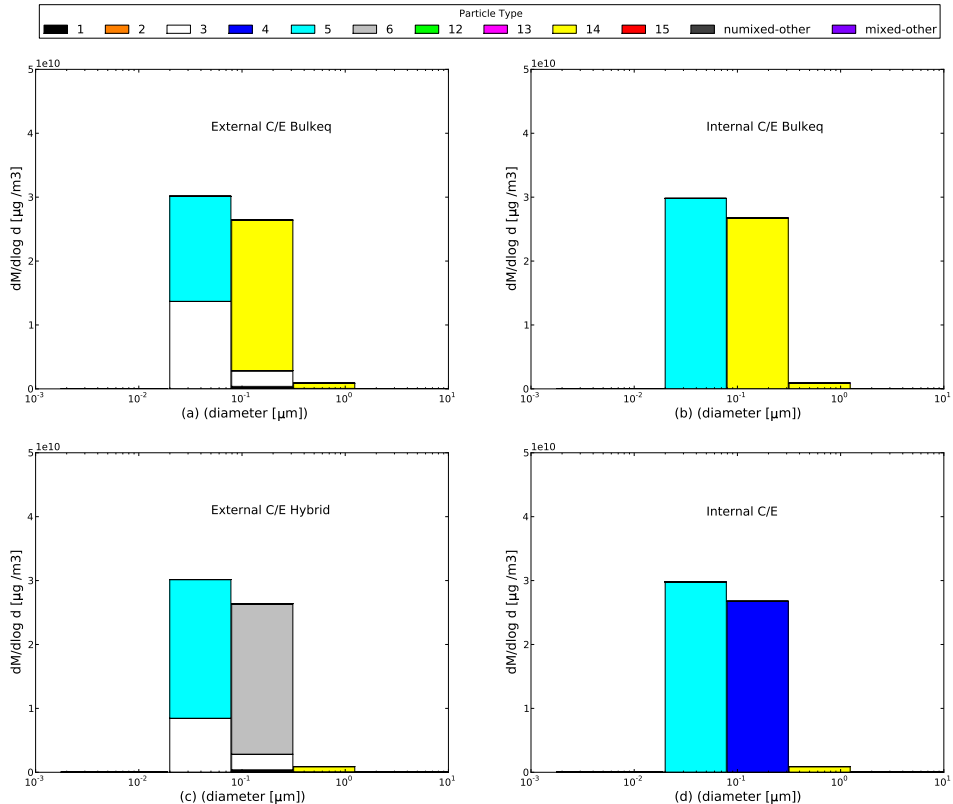


Figure 10. Result number distributions of externally-mixed particles as a function of particle diameter for the different chemical compositions for 4 different C/E simulation scenarios: (a) External bulk-equilibrium; (b) Internal bulk-equilibrium; (c) External hybrid method; (d) Internal dynamic.

Table 1. 20 Externally-mixed particle compositions

composition Index	Mixing state	Mass fraction of each groups (%)				
		HLI	HLO	HBO	BC	DU
1	unmixed(DU)	0-20	0-20	0-20	0-20	0-100
2	mixed	0-20	0-20	0-20	20-80	0-80
3	unmixed(BC)	0-20	0-20	0-20	80-100	0-20
4	mixed	0-20	0-20	20-80	0-20	0-80
5	mixed	0-20	0-20	20-80	20-80	0-60
6	unmixed(HBO)	0-20	0-20	80-100	0-20	0-20
7	mixed	0-20	20-80	0-20	0-20	0-80
8	mixed	0-20	20-80	0-20	20-80	0-60
9	mixed	0-20	20-80	20-80	0-20	0-60
10	mixed	0-20	20-80	20-80	20-80	0-40
11	unmixed(HLO)	0-20	80-100	0-20	0-20	0-20
12	mixed	20-80	0-20	0-20	0-20	0-80
13	mixed	20-80	0-20	0-20	20-80	0-60
14	mixed	20-80	0-20	20-80	0-20	0-60
15	mixed	20-80	0-20	20-80	20-80	0-40
16	mixed	20-80	20-80	0-20	0-20	0-60
17	mixed	20-80	20-80	0-20	20-80	0-40
18	mixed	20-80	20-80	20-80	0-20	0-40
19	mixed	20-80	20-80	20-80	20-80	0-20
20	unmixed(HLI)	80-100	0-20	0-20	0-20	0-20

Table 2. Mixing state after 12hs simulation

Process	No Dynamic	Coagulation	C/E	C/E+Coag+Nucl
	scenario (A)	scenario (B)	scenario (C)	scenario (D)
Mixed particle number (%)	42	79	48	51
Mixed particle mass (%)	83	85	64	76

Table 3. Computational times

Process	C/E	C/E bulk	C/E hybrid	Coag	C/E+Coag	C/E+Coag bulk	C/E+Coag hybrid
Internal mixing (s)	7.1	0.11	0.4	0.06	7.3	0.14	0.5
External mixing (s)	63.2	0.3	54.2	48.4	122.8	31.5	113